



City Research Online

City, University of London Institutional Repository

Citation: Cabrera-España, F. J., Kamuka, A., Khaled, A., Hameed, M. F. O., Obayya, S. S. A. & Rahman, B. M. A. (2024). Optical and electrical characterization of solar cell with nanowires mimicking antireflection coating layers considering axial and radial PN junctions. *Energy Science & Engineering*, doi: 10.1002/ese3.1722

This is the published version of the paper.

This version of the publication may differ from the final published version.

Permanent repository link: <https://openaccess.city.ac.uk/id/eprint/32628/>

Link to published version: <https://doi.org/10.1002/ese3.1722>

Copyright: City Research Online aims to make research outputs of City, University of London available to a wider audience. Copyright and Moral Rights remain with the author(s) and/or copyright holders. URLs from City Research Online may be freely distributed and linked to.

Reuse: Copies of full items can be used for personal research or study, educational, or not-for-profit purposes without prior permission or charge. Provided that the authors, title and full bibliographic details are credited, a hyperlink and/or URL is given for the original metadata page and the content is not changed in any way.



City Research Online:

<http://openaccess.city.ac.uk/>

publications@city.ac.uk

ORIGINAL ARTICLE

Optical and electrical characterization of solar cell with nanowires mimicking antireflection coating layers considering axial and radial PN junctions

Francisco J. Cabrera-España¹  | Abdullah Kamuka¹ | Awad Khaled² | Mohamed F. O. Hameed^{2,3} | Salah S. A. Obayya^{2,3} | B. M. Azizur Rahman¹ 

¹School of Science and Technology, University of London, London, UK

²Centre for Photonics and Smart Materials, Zewail City of Science and Technology, Giza, Egypt

³Mathematics and Engineering Physics Department, Faculty of Engineering, University of Mansoura, Mansoura, Egypt

Correspondence

Francisco J. Cabrera-España and B. M. Azizur Rahman, School of Science and Technology, City, University of London, London EC1V0HB, UK.
Email: Francisco.cabrera@city.ac.uk and b.m.a.rahman@city.ac.uk

Funding information

H2020 Marie Skłodowska-Curie Actions

Abstract

It has been well documented that the usage of a textured cover layer reduces reflection from the air-solar cell interface, which ultimately enhances the power conversion efficiency (PCE) of a solar cell. The most commonly used patterns, such as pyramids, micropillars, nanowires (NW), and nanoholes have been widely studied and optimized. Besides using such NWs to enhance light absorption, this work also additionally considers the concept of mimicking the antireflection coating of single or multiple layers in minimizing the reflectance and thus enhancing the total absorptance further. It is shown here that at least one order of magnitude shorter multilayer NW pattern of 268 nm total height can outperform a standard NW of 4270 nm height, which needs less material and can also be fabricated at a reduced cost. Furthermore, the proposed design with reduced height has a significantly lower surface-to-volume ratio, which also reduces surface recombination loss than the other textured surface patterns. The results presented in this work have been comprehensively analyzed by initially optimizing optical absorption and then completing the electrical simulations. The optimized design in conjunction with a back reflector offers an efficiency as high as 16.434%.

KEYWORDS

absorption enhancement, cost reduction, light trapping, nanowires, solar cell, texturing patterns

1 | INTRODUCTION

Although, in recent years, there has been an increasing interest in renewable energy generation driven by government policies and social awareness,^{1–6} the energy we still consume today is mostly generated from fossil fuels.⁷ However, photovoltaic solar cell (PVSC) is already

playing an even bigger role in cleaner energy generation. The sunlight is available to everyone and free to access and the current level of the technology involved is offering very promising performance.⁸

Since the discovery of PVSC in 1954 at the Bell Lab with only 6% power conversion efficiency (PCE),⁹ crystalline Silicon (c-Si) PVSCs have experienced a steady

This is an open access article under the terms of the [Creative Commons Attribution](https://creativecommons.org/licenses/by/4.0/) License, which permits use, distribution and reproduction in any medium, provided the original work is properly cited.

© 2024 The Authors. *Energy Science & Engineering* published by Society of Chemical Industry and John Wiley & Sons Ltd.

improvement to achieve 26.5%¹⁰ PCE for a single junction, almost reaching the Shockley-Queisser limit. However, as a 180–300- μm -thick costly c-Si layer is needed for near complete light absorption, which accounts for 40% of the cost,^{10,11} the payback time is rather long. To reduce the cost, second-generation PVSC explored 2–3- μm -thick thin-film but efficiency has been poor. Current third-generation solar cell research, dominated by thin organic perovskite-based PVSC, is showing good efficiency; however, its stability issue and use of toxic Pb need to be addressed before commercialization.

As the Si PVSC technology is very mature, *only* a reduction in its price will be the key to encourage its wider and faster adoption. But a thinner solar cell will also have a lower PCE. One of the techniques used to improve the efficiency of a thinner absorbing layer is texturing the surface of a thin Si PVSC with an array of geometrical patterns, such as pyramids,^{12,13} inverted pyramids,¹⁴ micropillar,^{15,16} nanowires (NW),^{17–19} nanoholes,^{20,21} NW with nanoholes,²² or plasmonic structure.^{23,24} The texturing technique effectively increases the number of times sunlight is incident on the solar cell due to multiple reflections between the elements of the pattern, which leads to an increase in absorption.^{12–17,25} It has been reported that the Lambertian limit of light trapping can be achieved by an ideal rough surface where incident light is randomly scattered, which increases the optical path length.²⁶ In this limit, for a Si NW, the optical path can be increased by $\approx 2n^2$, or around 25 times,²⁶ which can allow to reduce silicon wafer thickness from 200 to 300 μm to just 8–12 μm , nearly two orders of magnitude reduction, resulting in a significant potential cost reduction. The enhanced PCE by using textured or nanostructures has been experimentally validated. Singh et al.¹⁶ reported 16.4 PCE using only 3–4 μm NW and Lee et al.²⁷ and Choi et al.²⁸ have also reported 17.6% and 21.1% PCE, respectively using NWs. Nevertheless, the use of NWs can also be viewed as, instead of a single large silicon–air interface, by introducing two interfaces with two smaller refractive index changes and thus, by controlling the equivalent index of the middle layer.²⁹ Therefore, for the solar spectrum there will be an intermediate layer between air and the solar cell. Hence, following Fresnel's equation the total reflection from each of these two interfaces, air-textured pattern and textured pattern-solar cell is considerably reduced. This can lead to a higher fraction of the sunlight incident on the solar cell being absorbed in even a thinner active layer thus reducing the cost further.

The use of NW array texturing patterns has been widely reported due to its advantages over other texturing patterns. It offers a good absorption enhancement by increasing the effective light path and the optimized

device can be easily replicated using etching masks.^{17,29,30} These NW can be fabricated by using chemical etching³¹ or electron lithography.³² It should be noted that enhanced optical absorption may not always yield higher PCE as there may be other deteriorating factors, such as surface recombination. The effect of surface recombination can be minimized by using surface passivation techniques and by implementing a p-n radial junction.^{15,17,33,34} The use of radial junction reduces diffusion length²⁸ and also decouples^{35,36} the optical and electrical pathways of the active region allowing incident light to be absorbed in the axial direction while the carriers are collected in the radial direction.

Conventional NWs have a circular shape. Nevertheless, the design flexibility using mask etching technology enables the fabrication of NWs of different shapes, such as triangular, square, or hexagonal shapes, and even can be more exotic such as branched NW,³⁷ or quad-crescent NW,³⁸ flower-shaped NW,³⁹ and the moth-eye NW.⁴⁰ In this work, the authors first discuss the effect of shapes by analyzing the optical performance of NWs via the finite difference time domain (FDTD) method⁴¹ using the Lumerical FDTD-solutions package⁴² and by analyzing the electrical performance via the finite element method (FEM)⁴³ using the Lumerical DEVICE Charge package.⁴² This work suggests that the need for a costlier silicon layer can be further reduced by at least one order of magnitude compared to the traditional nanowire designs.

2 | OPTICAL SIMULATION SETUP

The basic schematic of the unit element included in the simulation window for the optical simulations is given in Figure 1. Here, we have considered a rigorous FDTD

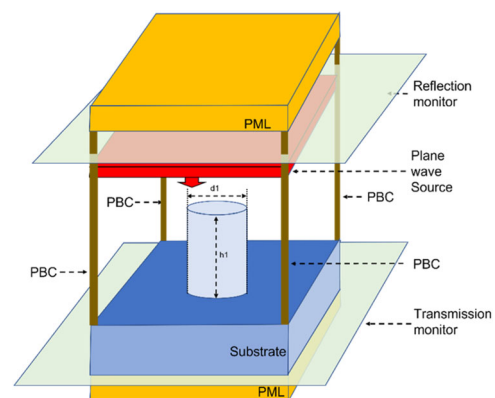


FIGURE 1 Schematic diagram of the setup for the optical simulation.

approach using Lumerical commercial software. A plane wave is launched, replicating the solar spectrum $I_{AM1.5}$ ⁴² and two monitors, shown by light green semi-transparent plates, measure the electromagnetic waves passing through them. One monitor is above the source to measure the electromagnetic waves reflected by the c-Si NW pattern where we used the refractive index for c-Si value from Palik,⁴⁴ available in the Lumerical material library.⁴² For consistency, the other monitor is placed at 4000 nm depth inside the c-Si substrate to measure the electromagnetic wave that is not absorbed by the pattern. The perfectly matched layers (PMLs) are used for the top and bottom horizontal boundaries to avoid spurious reflections from the computational boundaries by absorbing any electromagnetic waves reaching these boundaries. Additionally, on the four vertical side boundaries, the periodic boundary conditions (PBC) are considered to reduce the computational domain and also computational cost by representing an infinite array of solar cells by a single cell unit as shown in Figure 1.

3 | OPTICAL SIMULATION RESULTS AND DISCUSSION

First, we study the effect of different NW shapes by varying their dimensions. For a fair comparison, dimensions of noncircular NWs are represented by their equivalent diameter (dNW), when their cross-sectional areas are the same. Variations of the Absorption efficiency of all these shaped NWs with their equivalent dNW values between 40 and 300 nm for a unit cell of 300×300 nm are shown in Figure 2A. As the absorption also depends on the height of the NW (hNW), initially a fixed hNW of 2000 nm is considered. The NW shapes under consideration are: the conventional circular, triangular, rectangular, and hexagonal NWs. Along with these cases, results for a planar structure when no NW is used are also shown by a horizontal pink line, for

comparison. However, the reflection and absorption of optical energies are also wavelength-dependent. To ensure that we compare the total absorption (TABS) over the whole solar spectrum and not just only at a specific wavelength, we integrate the weighted absorbance over the whole solar spectrum as follows:

$$TABS = \frac{\int_{I_{AM1.5}} ((1 - T_{bottom}(\lambda) - T_{reflection}(\lambda)) \times I_{AM1.5}(\lambda)) d\lambda}{\int_{I_{AM1.5}} I_{AM1.5}(\lambda) d\lambda}, \quad (1)$$

where T_{bottom} , $T_{reflection}$, $I_{AM1.5}$, and λ are the transmission of electromagnetic waves reaching a depth of 4000 nm within the substrate, the transmission of electromagnetic waves reflected by the solar cell surface, the irradiance of the reference solar spectrum AM 1.5, and the wavelength, respectively.

In the literature, designs incorporating various shapes of NWs have been considered, but as the absorption also critically depends on their cross-sectional area, a normalized dimension is used here to compare their performances more fairly, each having the same cross-sectional area. Variations of the TABS with the equivalent diameter of the NW are shown in Figure 2A. It can be observed that the TABS values for NWs of any shape or size are significantly higher than 0.461, that of a planar case, shown by an orange horizontal line. Furthermore, it can also be observed that the values of TABS for shorter diameters are smaller but as their equivalent dNW increases, the overall TABS increases. Then, for dNW larger than 140 nm, their performance stabilizes and remains approximately constant for dNW values up to 180 nm. Within this range of diameters (i.e., 140–200 nm), it may be observed that TABS for different shapes are nearly the same, which suggests that they are almost shape-independent but strongly depend on their equivalent dNW. Their maximum TABS values, at

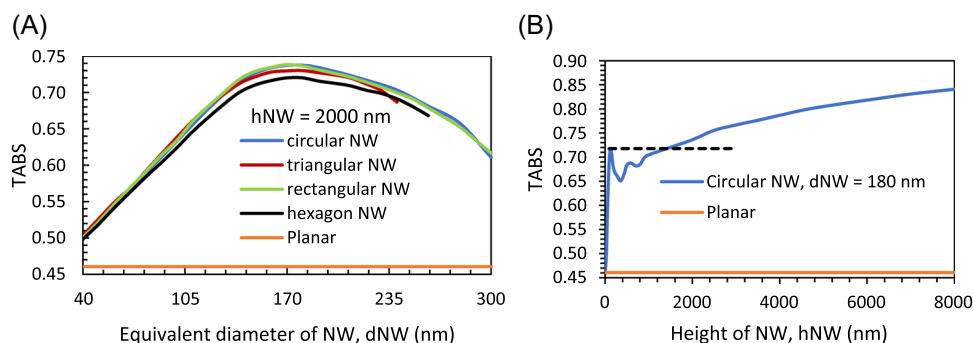


FIGURE 2 (A) Variations of total absorption (TABS) with equivalent dNW for different nanowires (NW) shapes, (B) variations of TABS with the NW height for a circular NW of dNW = 180 nm.

dNW = 180 nm are 0.72, 0.73, 0.736, and 0.737 for hexagonal, triangular, rectangular, and circular-shaped NW, respectively. This shows that the performance of NW depends on their size but not on their shapes, which agrees with an earlier similar observation. This also clearly shows that by introducing NW the overall TABS can be 60% improved, which is almost shape-independent. Moreover, it is strongly dependent on the cross-sectional area covered by NWs, which is an indication of the equivalent refractive index of the NW layer and can be calculated by Rytov's formula.⁴⁵ This suggests that there is an optimum equivalent dNW or optimum equivalent index of that layer and further increases in the diameter lead to a decrease in the value of TABS.

Nevertheless, as it has been well documented by other researchers, the benefit in the absorption efficiency of placing an NW on the surface of a solar cell is not only dependent on the diameter but also on the height. Figure 2B shows the effect of height on TABS of a circular NW of dNW = 180 nm with hNW increasing from 25 to 8000 nm by a blue line and compares the performance with a planar solar cell without any NW. It can be observed that at the start as the hNW increases TABS also increases rapidly. Following that, TABS increases slowly as the hNW increases further. This suggests that for a given NW of any diameter, it is possible to obtain a higher TABS by simply increasing its height. This would also suggest that to obtain a higher TABS, the height of the NW and so also the amount of Si used in the NW will need to be increased, but this will also raise the costs. Additionally, this also has the direct consequence of increasing the surface-to-volume ratio of the pattern, which is expected to diminish the electrical performance of the cell due to the increased surface recombination.

In Figure 2B, a ripple is also noticeable in the shorter hNW range, which has often been ignored in the aim to get much higher efficiency using much taller NWs. This ripple indicates that using relatively very short NWs it is possible to obtain a TABS value as high as that can be offered by a moderately taller NW. For instance, the local maximum TABS value (TABS = 0.718) in the ripple is obtained using NW of only 130 nm high but to get the same TABS value a NW needs to be hNW = 1450 nm high, shown by a black dashed line. We will show that this is linked to the equivalent refractive index and the $\lambda_g/4$ concept applicable in antireflection coating (ARC) layers, where $\lambda_g(\lambda) = \lambda/n(\lambda)$ is the wavelength of the electromagnetic wave inside the medium and n is the refractive index of the material or the equivalent material.

To validate this concept, we have carried out simulations for a simple homogenous layer with

optimum refractive index (n_{opt}) on the top of the Si solar cell as an ARC layer and analyze the reflectance while varying its thickness. The n_{opt} of a single layer ARC minimizing the reflectance at an interface is well documented to be the geometric average between the refractive index of the air and that of the substrate (i.e., $n_{\text{opt}} = \sqrt{n_{\text{Si}}}$, where n_{Si} is the refractive index of Si in our case^{46,45}).

Variations of reflectance, R with the wavelength are shown in Figure 3 for two different ARC thicknesses, 100 and 120 nm. From Figure 3, it can be observed that there is near zero reflectance at wavelength 750 nm when $t = 100$ nm, shown by a blue line. At wavelength 750 nm, the refractive index value of silicon, $n_{\text{Si}} = 3.7237$, so, $\sqrt{n_{\text{Si}}} = 1.9297$. Hence, λ_g inside the ARC layer is 388.66 nm at this wavelength. In this case, at $\lambda_0 = 750$ nm, the 100-nm-thick ARC layer is equivalent to $0.2573 \lambda_g$. This is in line with the concept of achieving minimum reflectance when the thickness of the layer is equal to $m\lambda_g/4$, when m is an odd integer. However, from basic optics theory we also know that besides the minimum reflectance at an interface with a layer of thickness equal to $\lambda_g/4$, there is also an associated peak reflectance at a shorter wavelength where the thickness is equal to $m\lambda_g/2$, when m is an integer.⁴⁷ In the case of $t = 100$ nm it can be observed that there is a peak at wavelength 430 nm. At $\lambda_0 = 430$ nm, the 100-nm-thick ARC layer is equivalent to $0.512 \lambda_g$ (note that, $\sqrt{n_{\text{Si}}}$ at $\lambda_0 = 430$ nm is 2.20003) which is again in line with the concept of achieving peak reflectance when the thickness of the intermediate layer equals $\lambda_g/2$. Similarly, in the case of the $t = 120$ nm, the minimum reflectance is at $\lambda_0 = 900$ nm where $t \cong 0.25\lambda_g$ and the peak reflectance is at $\lambda_0 = 490$ nm where $t \cong 0.5\lambda_g$. Therefore, an ARC layer can be designed to minimize reflectance at any given wavelength, which will increase absorption. However, it is also clear that when considering the solar spectrum only a very narrow wavelength range will be benefited

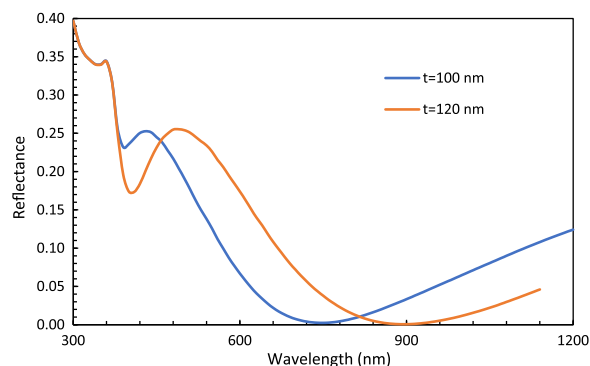


FIGURE 3 Variations of reflectance with the wavelength for single-layer antireflection coating.

from the minimum reflectance. This implies that there can be a compromise where we accept minimum reflectance at the cost of higher reflectance at other wavelengths. However, to make this compromise, we first need to identify the wavelength at which we should optimize the performance. Also, we need to bear in mind that these curves were obtained from simulations considering the optimized refractive index for the ARC layer. In reality, it will be difficult to find any low-loss material with a refractive index that may be close to $\sqrt{n_{\text{Si}}}$. Besides this, even if it is possible to find such a material at any particular wavelength, it would be difficult to achieve this over the whole solar spectrum due to strong material dispersion. However, this optimum refractive index ($\sqrt{n_{\text{Si}}}$) can be artificially replicated as closely as possible by controlling *only* the cross-sectional area of the NW. As described above, the diameter of the NWs defines the equivalent refractive index of the pattern. By mimicking the ARC, we can take advantage of better performance with a shorter NW where the ripple was observed in the Figure 2B.

As a proof of concept, variations of the TABS with the dNW for 2 hNWs, 1450 and 130 nm (i.e., height offering the peak of the ripple) are shown in Figure 4. A strong correlation can be observed between Figures 2b and 4 since both curves in Figure 4 show almost similar performance. When increasing dNW, both curves in Figure 4 have a similar rate of increase in the value of TABS in the shorter diameter range. At dNW = 180 nm, both the NWs have the same TABS value, which confirms their equal values in Figure 2B when dNW was fixed at 180 nm. Furthermore, both lines have very similar peak TABS values. In the case of $h = 1450$ nm, the maximum TABS of 0.721 is obtained when dNW = 180 nm, and in the case of $h = 130$ nm, the maximum TABS of 0.725 is obtained when dNW = 200 nm. This is especially remarkable considering that there is a large difference in their heights and thus also in their surface-

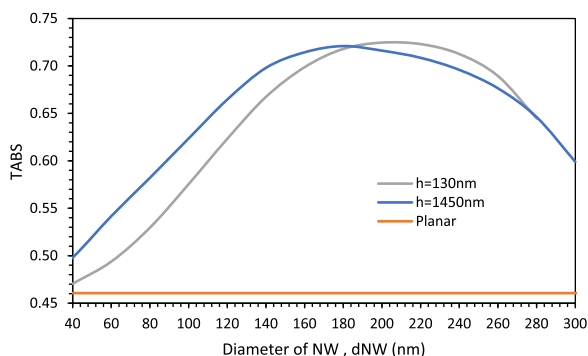


FIGURE 4 Variations of total absorption (TABS) with the dNW for the case of 1NW antireflection coating.

to-volume ratios. This leads us to believe that within the range of height of NWs offering the ripple (i.e., between $h_{\text{NW}} = 50\text{--}400$ nm), it is possible to treat the NW pattern mimicking a single optimized ARC layer where the diameter defines the equivalent refractive index of the ARC layer. Hu et al.⁴⁸ have reported for 5- μm -high GaAs NWs, with 180 nm diameter and 350 nm pitch offering the best absorption and suggested possibly due to current matching. Kupec et al.⁴⁹ have discussed in terms of their geometric fill-factor and reported similarly for 1000 nm high Indium Phosphide (InP) NW with 180 nm diameter and 360 nm pitch offering the best light absorption. Yan et al.⁵⁰ reported for a fixed $d/\Lambda = 0.5$, the best absorption for 2- μm -high GaAs NWs was with $d = 310$ nm. We have also observed that as the pitch is increased, the diameter needs to be increased to obtain maximum TABS. However, in case, the diameter is kept constant, say at 200 nm with a fixed height of 130 nm, the maximum TABS value of 0.725 was obtained when pitch was 300 nm. After that, the TABS value monotonically decreased as expected since the equivalent refractive index of the unit cell was also reduced, and its TABS value reduced to only 0.487 when the pitch was 1000 nm. Further, an increase in the pitch will asymptotically reach the minimum TABS value of 0.461, the same as that of a planar surface without any NW.

As mentioned above, the ideal refractive index for a single-layer ARC to minimize the reflectance at the air-Si interface is $\sqrt{n_{\text{Si}}}$. However, from the basic principles given by Fresnel's equation, we are aware that we can further minimize the reflectance by considering two layers of ARC instead of one. In this case, the upper ARC layer needs to have a refractive index equal to $\sqrt[3]{n_{\text{Si}}}$ and the lower ARC layer needs to have a refractive index equal to $\sqrt[3]{n_{\text{Si}}^2}$. It is easy to adjust the equivalent index of a layer by just varying the diameter of the NW. We present the results after introducing a second narrower NW, placing it on top of the lower NW and always keeping the upper NW (NW2) with a diameter smaller than that of the lower NW (NW1). Figure 5A illustrates the NW pattern equivalent to a two-layer ARC.

Next, an iterative approach is considered to optimize the four variables d_1 , d_2 , h_1 , and h_2 to maximize the TABS. In each iteration, only one parameter is varied at a time while others remain constant at their optimized values. After three complete iterations, these parameters are identified as, $d_1 = 254$ nm, $d_2 = 150$ nm, $h_1 = 130$ nm, and $h_2 = 90$ nm. The effect of their widths and heights is shown in Figure 6. Figure 6A shows the variation of the TABS with d_1 by a blue curve when fixed $d_2 = 150$ nm, $h_1 = 130$ nm, and $h_2 = 90$ nm are used. It can be observed here that the maximum TABS obtained is 0.769 when $d_1 = 254$ nm. Variations of the TABS with d_2 are shown

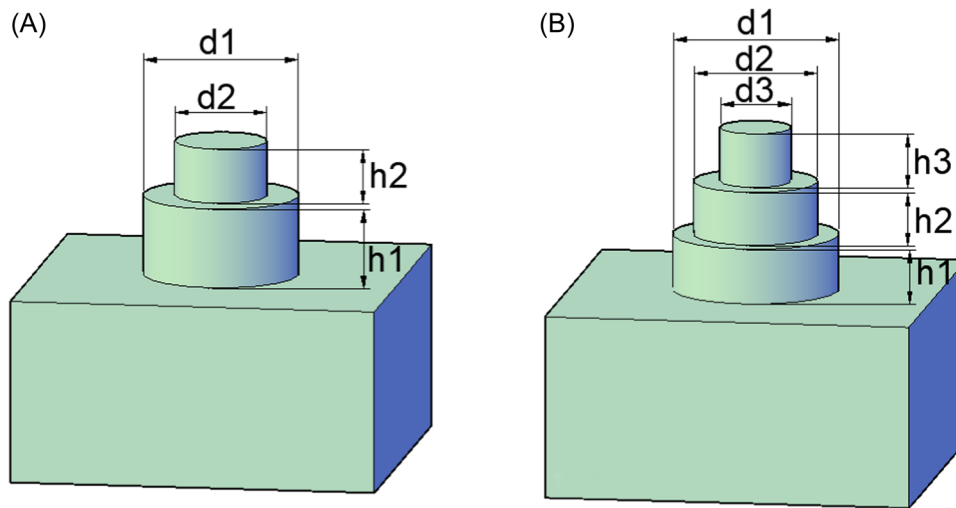


FIGURE 5 Schematic diagram (A) for the 2NW antireflection coating (ARC) design and (B) for the 3NW ARC design.

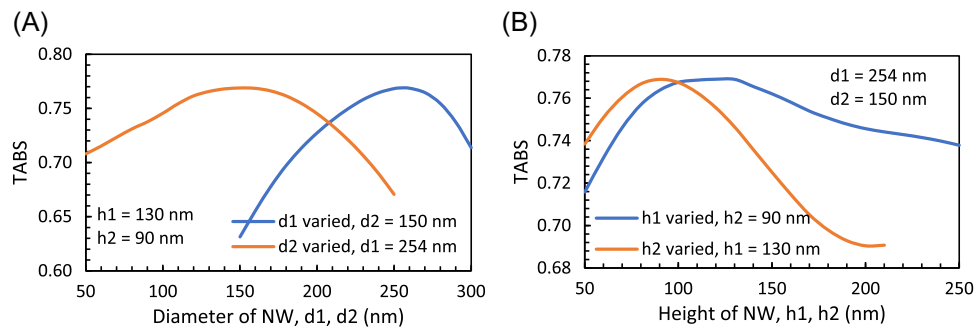


FIGURE 6 (A) Variations of total absorption (TABS) with the diameter of two layers of equivalent antireflection coating (ARC). (B) Variations of TABS with the height of two layers of equivalent ARC.

by an orange curve with fixed $d_1 = 254$ nm, $h_1 = 130$ nm, and $h_2 = 90$ nm. It can be observed here that the same maximum TABS is 0.769 when $d_2 = 150$ nm. The maximum TABS value of 0.769 obtained when using the two NW ARC design represents a significant increase compared to the maximum TABS observed when a single NW layer was considered with its maximum TABS = 0.729 as shown earlier in Figure 4 at $h = 130$ nm. Figure 6A shows clearly the effect of changing the diameter of each of the NWs. Both curves show a similar trend, the TABS increases with the diameter reaching a peak value and then decreases for larger diameters. The optimum value of d_1 (254 nm) is larger than the value of d_2 (150 nm). This is consistent with the idea of mimicking two ARC layers since the equivalent refractive index of NW1 needs to have a value close to $\sqrt[3]{n_{\text{Si}}^2}$ and the equivalent refractive index of NW2 needs to have a value close to $\sqrt[3]{n_{\text{Si}}}$ to minimize reflectance. As $\sqrt[3]{n_{\text{Si}}^2}$, the refractive index of the lower layer is higher than $\sqrt[3]{n_{\text{Si}}}$,

the refractive index of the upper layer, d_1 needs to be larger than d_2 , as demonstrated here.

Figure 6B shows the variations of TABS with the height of the NWs, h_1 , and h_2 , while keeping the other parameters constant at the already optimized values, $d_1 = 254$ nm, $d_2 = 150$ nm, $h_1 = 130$ nm, and $h_2 = 90$ nm. It can be observed that as h_1 is increased, shown by a blue line, initially TABS increases, reaching its maximum value of 0.769 when $h_{1,\text{opt}} = 130$ nm. Similarly, when h_2 is varied, as shown by an orange line, initially TABS increases, reaching its maximum value of 0.769 when $h_{2,\text{opt}} = 90$ nm. Moreover, when comparing the peak TABS values in Figure 6B, it should be noted that, when two layers of equivalent ARC are used, a combined height of only 220 nm can achieve as high a TABS value as that of a simple NW with a height at least 3450 nm (can be found from Figure 2B). It should be noted that the NW heights do not correspond to any specific $\lambda_g/4$, as maximum TABS is obtained by integrating over the whole solar spectrum. This is a clear indication of the

superior optical performance of the concept proposed in this work.

Similar two-layer NWs with lower and upper diameters, 130 and 60 nm, respectively but with 1 μm height each (2 μm total height) in Ge PVSC⁵¹ have been fabricated by controlling the etching time. Their work reported more than double the absorption compared to that using a 2- μm -thick planar layer. They have suggested this may be due to possible impedance matching. Wendisch et al.³¹ have also reported similar two diameters Si NWs, with upper and lower diameters of 98 and 133 nm with their heights of 1340 and 590 nm, respectively, fabricated by sequential metal-assisted chemical etching (MACE) and KOH etching. Their simulated and experimentally measured results showed a large increase in absorption. So, it can be concluded that this concept of progressively narrowed dual diameter NWs is feasible to fabricate, and have shown experimentally validated results improving light absorption. However, our paper reports that by additionally optimizing their heights, higher TABS value can be obtained at a rather lower height, the main focus of this work, which would have a significant advantage in reducing the material cost.

Furthermore, the excellent performance offered by this design can be further enhanced by introducing an additional NW on top of the previous two NWs (i.e., NW3) as illustrated in Figure 5B. In this case, the equivalent refractive index of NW1, NW2, and NW3 should be $\sqrt[4]{n_{\text{Si}}^3}$, $\sqrt[4]{n_{\text{Si}}^2} = \sqrt{n_{\text{Si}}}$, and $\sqrt[4]{n_{\text{Si}}}$, respectively.

Next, an iterative approach is considered to optimize the six variables to maximize TABS (i.e., d_1 , d_2 , d_3 , h_1 , h_2 , and h_3). After iterating all six parameters for three complete cycles, the optimized values obtained are $d_1 = 272$ nm, $d_2 = 203$ nm, $d_3 = 116$ nm, $h_1 = 91$ nm, $h_2 = 88$ nm, and $h_3 = 89$ nm. The effect of each parameter, keeping the other five parameters fixed at their optimized values, is shown in Figure 7A. Figure 7A shows the variation of TABS with d_1 , the diameter of the

bottom-most layer by a blue line. It can be observed that as d_1 increases, the value of TABS increases reaching its maximum of 0.785 when $d_1 = 272$ nm. The variation of TABS with d_2 , the diameter of the middle layer, is shown by an orange line. It can be observed that as d_2 increases, the rate of increase is slightly more pronounced than in the case of d_1 , reaching the maximum of 0.785 when $d_2 = 203$ nm. The variation of TABS with d_3 , the diameter of the top-most layer, is shown by a gray line. It can be observed that as d_3 increases, the rate of increase is less pronounced than in the cases of d_1 and d_2 , reaching its maximum TABS value of 0.785 when $d_3 = 116$ nm. Therefore, the smallest optimized diameter is d_3 (lowest equivalent refractive index), followed by d_2 (medium equivalent refractive index), and finally d_1 (highest equivalent refractive index). This is consistent with the expected equivalent refractive index values from ARC layer theory where $\text{NW3} \rightarrow \sqrt[4]{n_{\text{Si}}}$ (lowest), $\text{NW2} \rightarrow \sqrt[4]{n_{\text{Si}}^2} = \sqrt{n_{\text{Si}}}$ (medium), and $\text{NW1} \rightarrow \sqrt[4]{n_{\text{Si}}^3}$ (highest). Therefore, from Figure 7A it can be observed that by including the third NW and optimizing its performance, it is possible to improve the value of TABS from 0.769 (2NWs ARC case) to 0.784 (3NWs ARC case). Although the improvement is modest, such a value of TABS can only be achieved when a single NW of height 4270 nm is used, which is significantly taller.

Variations of TABS with the heights of NWs (h_1 , h_2 , and h_3) are shown in Figure 7B while keeping the other parameters fixed at their already optimized values of $h_1 = 91$ nm, $h_2 = 88$ nm, $h_3 = 89$ nm, $d_1 = 272$ nm, $d_2 = 203$ nm, and $d_3 = 116$ nm, as needed. Variation of the TABS with the height of the bottom NW, h_1 is shown by a blue line. It can be observed that TABS rapidly increases from 0.742 when $h_1 = 30$ nm to its maximum value of 0.785 when $h_1 = 91$ nm. Variation of the TABS with the height of the middle NW, h_2 is shown by an orange line. It can be observed that the value of TABS increases at a slower rate with increasing h_2 compared to when increasing h_1 . The value of TABS increases from

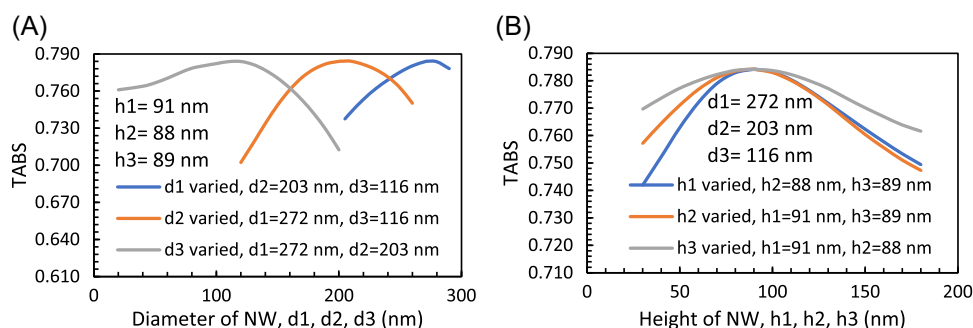


FIGURE 7 (A) Variations of total absorption (TABS) with the diameter of three layers of equivalent antireflection coating (ARC). (B) Variation of TABS with the height of three layers of equivalent ARC.

0.757 when $h_2 = 30$ nm to 0.785 when $h_2 = 88$ nm. Variation of the TABS with the height of the top-most NW, h_3 is shown by a gray line. It can be observed that the value of the TABS increases from 0.769 when $h_3 = 30$ nm to 0.785 when $h_3 = 89$ nm. Therefore, the optimized height for the bottom-most NW is $h_1 = 91$ nm, for the middle NW is $h_2 = 88$ nm, and for the top-most NW $h_3 = 89$ nm where they all converge toward the same maximum value. In the calculation of TABS, we integrate the total absorption over the whole wavelength range of the solar spectrum. Hence, this gives an averaging height, which is nearly wavelength-independent, and for all three layers, their heights are nearly similar. In any case, it is worth highlighting that the optimized total thickness for the case of the three-layer NW ARC design, only 268 nm, can achieve a TABS value of 0.785. However, if instead of the three-layer NW ARC design, a simple NW layer is used, then it would require an NW height of 4270 nm, which will also need more Si being used and hence incur higher costs. We have also evaluated PVSC with more than three ARC layers, but the observed benefit was very small and thus this is not shown here.

We have calculated the equivalent index values of NWs for different optimized diameters using Rytov's equation for the optimized three NWs, two NWs, and single NW ARC layers. Figure 8 illustrates the correlation between the equivalent refractive index calculated for each case, with the ideal refractive index values needed for these layers to satisfy the antireflection conditions. For the three layers case, these ideal values are, NW1 $\rightarrow \sqrt[4]{n_{Si}^3}$, NW2 $\rightarrow \sqrt[4]{n_{Si}^2} = \sqrt{n_{Si}}$, and NW3 $\rightarrow \sqrt[4]{n_{Si}}$, shown by three hollow blue squares, for the two layers case, NW1 $\rightarrow \sqrt[3]{n_{Si}^2}$ and NW2 $\rightarrow \sqrt[3]{n_{Si}}$, shown by two solid green triangles, and for the one layer case, NW1 $\rightarrow \sqrt{n_{Si}}$ shown by a red circle. However, as these refractive indices of highly dispersive Si are also dependent on wavelength, we have shown this only at a wavelength of

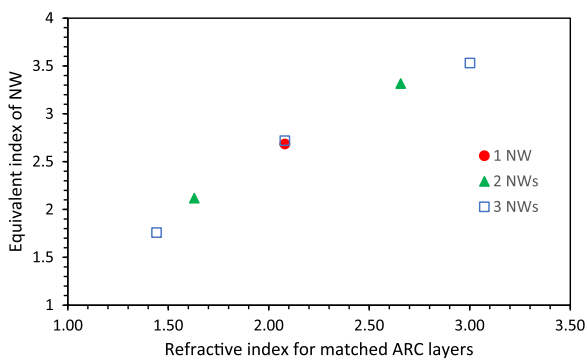


FIGURE 8 Equivalent refractive index of 3NWs antireflection coating (ARC) at wavelength 495 nm versus optimum refractive index needed for ARC at a wavelength 495 nm.

495 nm. A strong correlation between the two sets of these refractive index values can be observed in Figure 8. It is especially meaningful that the refractive index value for the case of 1NW is very close to the value for the middle layer of the 3NWs case. This is as expected since both cases are targeting to have a refractive index value equal to $\sqrt{n_{Si}}$. This is a strong indicator of the potential ability of the designed 3NWs pattern to act as a three-layer ARC using ideal refractive indexes for each of the three layers. It should be noted that equivalent refractive index or characteristic impedance are related to the fill-factor and these parameters are broadly shape-independent. But in this work, we have first rigorously optimized these designs by varying the dimensions of the NWs and shown later that these values closely correlate with the required refractive index values of the ARC layers.

Figure 9 shows the variation of absorptance with the wavelength for the cases of (i) a planar surface, shown by a black line (with total normalized absorptance, TABS = 0.4606), (ii) a simple NW pattern of 130 nm height and 180 nm diameter (TABS = 0.718), shown by a green line, (iii) the optimized 2NWs ARC pattern (TABS = 0.769), shown by a light blue line, and (iv) the optimized 3NWs ARC pattern (TABS = 0.784), shown by a red line. It can be observed that the improvement in the absorptance when a short NW is placed on the solar cell surface is significant over the whole solar spectrum when compared with a planar surface case. This improvement is then further enhanced when considering our designs on the solar cell surface, especially in the shorter wavelength range (300–700 nm), more particularly where the peak of the solar spectrum (i.e., $\lambda_{\text{peaksolar}} = 495$ nm) exists. In the case of the 2NWs ARC design, the absorptance around the shorter wavelength range is over 0.9. However, by introducing the 3NWs ARC design it is possible to reach an absorptance close to 1.

The optical performance of NWs can be discussed in terms of the frequency-domain mode field of the uniform

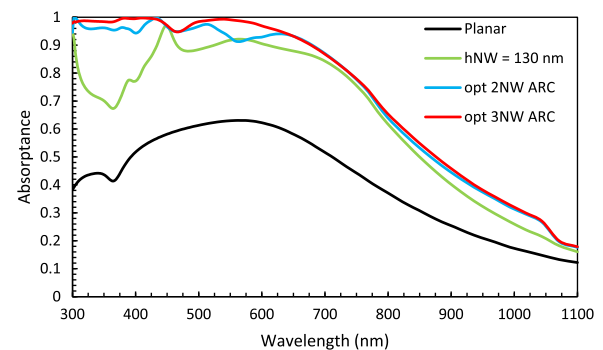


FIGURE 9 Variations of absorptance with the wavelength.

2-D waveguides, which is weakly wavelength-dependent, or 3-D resonating structures, which are strongly wavelength-dependent. It can also be evaluated in terms of the total field for a given excitation using a time-domain approach. We have considered them all, but here some total fields obtained by using 3D Lumerical simulations at some specific wavelengths are shown. Figure 10A–C shows field plots across the cross section in the x - z and x - y planes at different z positions of the simple NW of 130 nm height. The H_y field intensity contour along the x - z plane at $y = 0$ (i.e., center of the NW) when the operating wavelength is 497 nm is shown in Figure 10A. The white line represents the contour of the NW outlines. It can be observed that there are two weak side lobes at around $z = -290$ nm. Furthermore, the highest H_y intensity concentration is in the center of the NW at around $z = -367$ nm. This is an indication of a strong absorption of the design at 497 nm wavelength. The H_y field intensity contour along the x - y plane at $z = -367$ nm (inside the substrate, just below the NW) when the operating wavelength is 497 nm is shown in

Figure 10B. It can be observed that there is a very high H_y field intensity at the center. This is a clear illustration of the absorption capacity of short NWs. The E_x field intensity contour along the x - y plane at $z = -367$ nm (inside the substrate, below the NW) when the operation wavelength is 497 nm is shown in Figure 10C for a single NW ARC design. It can be observed that the E field intensity is very well concentrated at the center of the structure. There is barely any other E-field intensity peak. This is a further indication of the strong absorption of sunlight that can be absorbed within the Silicon substrate.

Figure 11A,B shows field plots along the x - z and x - y planes of the 2NWs ARC design. Figure 11A shows the H_y field intensity along the x - z plane when $y = 0$ (i.e., along the center of the NW) at operation wavelength 497 nm for a 2NW ARC design. The white lines represent the layout of the 2NWs ARC design. It can be observed that there is one main intensity peak at $z = 180$ nm (i.e., inside NW2) but with three peaks at $z = -305$ nm (inside NW1). It can be noted that at $z = -305$ nm, inside the

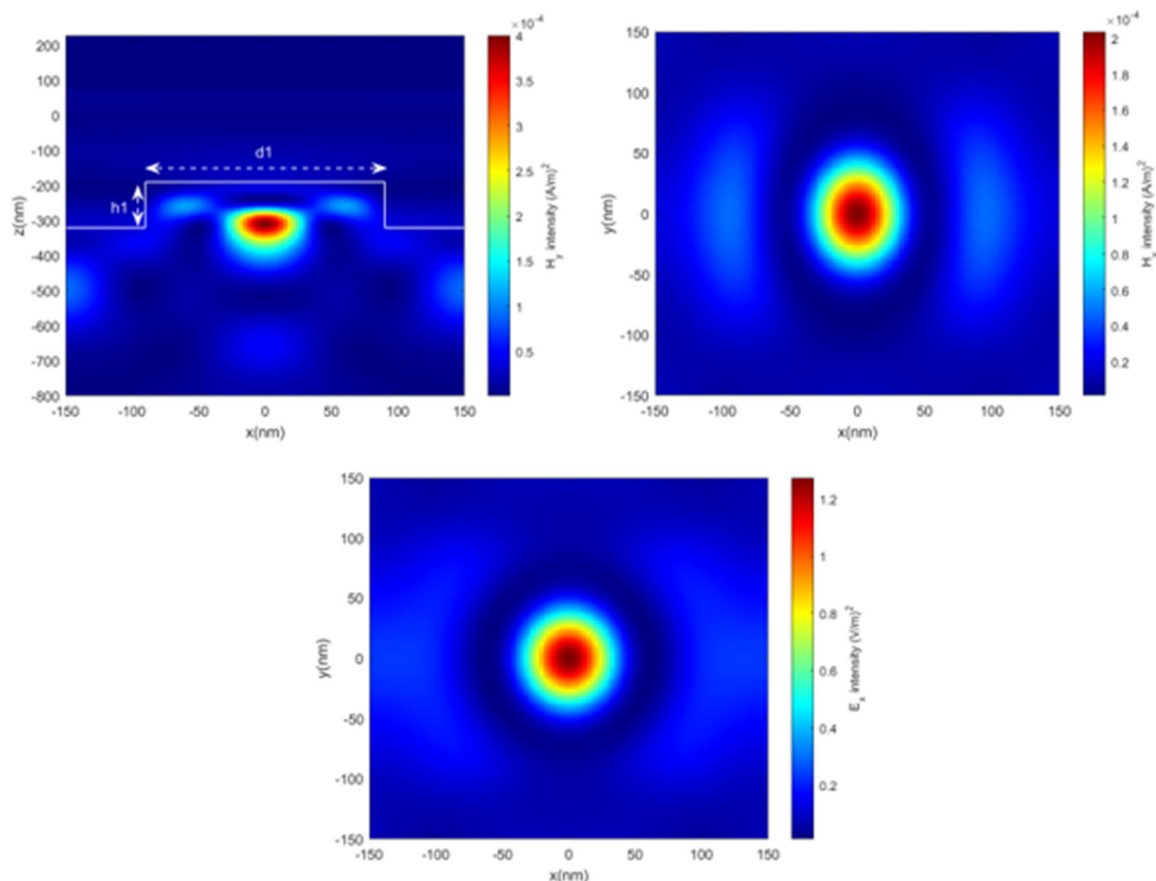


FIGURE 10 (A) H_y field intensity along the x - z plane when the operating wavelength is 497 nm—cutting center—simple NW for $h_1 = 130$ nm and $d_1 = 180$ nm. (B) H_y field intensity along the x - y plane when the operating wavelength is 497 nm at $z = -367$ nm for $h_1 = 130$ nm and $d_1 = 180$ nm - simple NW. (C) E_x field intensity along the x - y plane when the operating wavelength is 497 nm at $z = -367$ nm for $h_1 = 130$ nm and $d_1 = 180$ nm - simple NW.

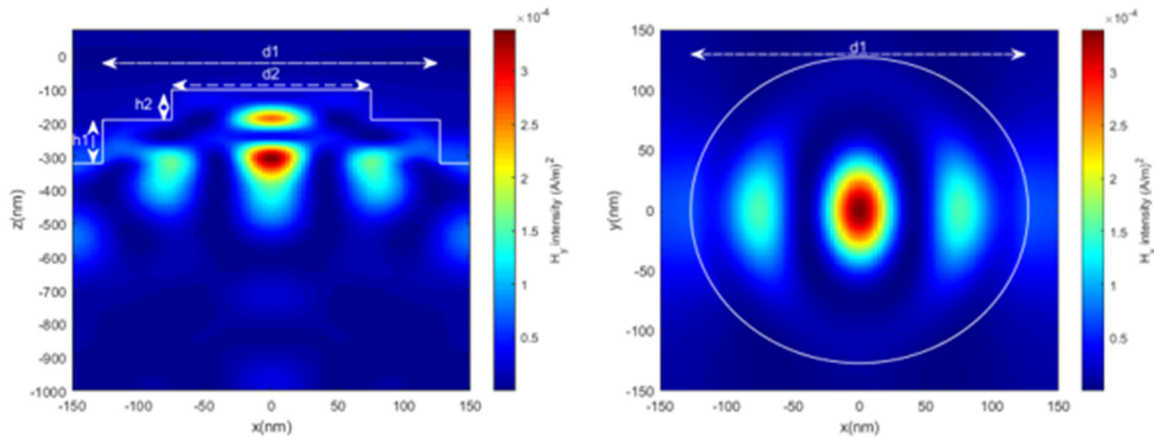


FIGURE 11 (A) H_y field intensity along the x - z plane when the operating wavelength is 497 nm for the optimum 2NWs antireflection coating (ARC) layer. (B) H_y field intensity along the x - y plane when the operating wavelength is 497 nm at $z = -305$ nm for the optimum 2NWs ARC layer.

lower and wider NW, the two peaks at the sides are smaller than the dominant peak at the center of the NW (at $x=y=0$). This is more clearly shown in Figure 11B. Furthermore, the dominant intensity peaks in Figure 11A suggest that each of the NWs is contributing to absorption. Therefore, the combined total absorption is higher. Additionally, there are two side lobes of lower intensity as observed in Figure 10A. Furthermore, when comparing Figure 11A with Figure 10A, a higher H field intensity concentration inside the 2NWs ARC design can be observed. This is a strong illustration of the superior optical performance of our design. Figure 11B shows the H_y field intensity along the x - y plane at $z = -305$ nm (inside NW1) when the operating wavelength is 497 nm for a 2NWs ARC design. Compared to Figure 10B it can be clearly observed here that the main dominant peak is at the center of the NW and then, there are two side lobes of moderate intensity on both sides. This means that the unique structural nature of the 2NWs ARC design enhances the absorption of sunlight from within the pattern itself. This leads to a higher number of electron-hole pairs, which then penetrate further into the substrate.

Figure 12A–E shows field contour plots along the x - z and x - y planes at different heights of the 3NWs ARC design. Figure 12A shows the H_y field intensity in the x - z plane when $y=0$ (i.e., center of the NW) and the operating wavelength is 497 nm for 3NWs ARC design. The white lines represent the sides of the 3NWs ARC design. It can be observed that there are three dominant intensity peaks at the center of the design at $z = -404$ nm (inside the substrate, just below NW1), at $z = -185$ nm (inside NW2), which is the peak of the highest intensity and at $z = -113$ nm (inside NW3). This is an indication that each of the three NWs contributes to the total

absorption. Therefore, the total absorption performance of the 3NWs ARC is superior to that of simple NW and 2NWs ARC designs. Additionally, we can observe that there are two side lobes of a lower intensity within NW1 and another two side lobes with peak intensity at $z = -320$ nm (just at the boundary between NW1 and the substrate). When comparing Figure 12A with Figure 10A and Figure 14A, a higher H field intensity concentration inside the 3NWs ARC design can be observed, which is the reason why the 3NWs ARC offers a superior optical performance. Figure 12B shows the E_x field intensity along the x - y plane at $z = -113$ nm (inside NW3) and the operating wavelength is 497 nm wavelength for a 3NWs ARC design. The white line represents the edge of the narrow NW3. In Figure 12B, an E_x field intensity concentration at the outer boundary of the upper NW (NW3) along $y=0$ can be observed. We have used periodic boundary conditions to model a unit solar cell. Along the boundary in the y -direction, the electric wall boundary condition was implemented. This is equivalent to the Neumann boundary condition for the E_x component at this wall (here shown as two vertical sides), which makes the \mathbf{E} field normal to the y -axis, and Dirichlet boundary conditions force the E_x field to be zero on the boundaries parallel to the x -axis (here shown as two horizontal sides). The high-intensity peaks outside NW3 are an indication of waves being incident on the side wall of NW3, which has been previously bounced at another interface of the pattern. Further to this, we can also observe that in the center of NW3, there is a weak E_x field intensity, indicating the absorption of light. Figure 12C shows the E_x field intensity along the x - y plane at $z = -185$ nm (inside NW2) when the operation wavelength is 497 nm for 3NWs ARC design. The white line represents the boundary of NW2. From Figure 12C it

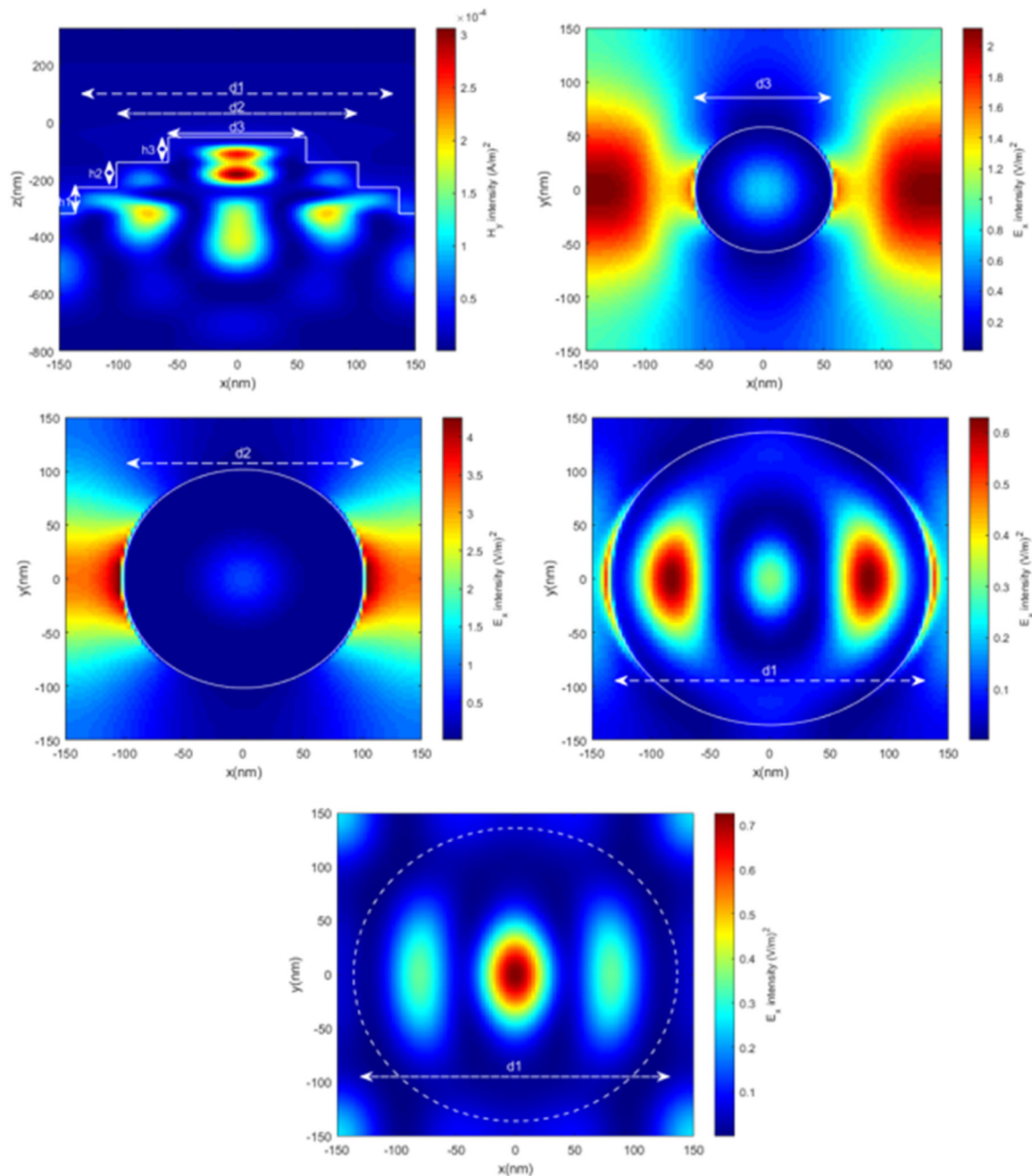


FIGURE 12 (A) H_y field intensity along the x - z plane when the operating wavelength is 497 nm for the optimum 3NW antireflection coating (ARC) layer. (B) E_x field intensity along the x - y plane when the operating wavelength is 497 nm at $z = -113$ nm for the optimum 3NW ARC layer. (C) E_x field intensity—along the x - y plane when the operating wavelength is 497 nm at $z = -185$ nm for the optimum 3NW ARC layer. (D) E_x field intensity along the x - y plane when the operation wavelength = 497 nm at $z = -320$ nm for the optimum 3NW ARC layer. (E) E_x field intensity along the x - y plane when the operation wavelength = 497 nm at $z = -404$ nm for the optimum 3NW ARC layer.

can be observed there is a higher \mathbf{E} field intensity concentration outside the NW, compared with what was observed in Figure 12B which indicates absorption of a larger portion of light in Fig. 12C. Further to this, we can also observe the high-intensity peaks outside the NW, which is an indication of waves being incident on the side wall of the NW from multiple reflections between adjacent NWs. Figure 12D shows the E_x field

intensity along the x - y plane at $z = -320$ nm (right at the boundary between NW1 and the substrate) when the operating wavelength is $\lambda = 497$ nm for 3NWs ARC design. The white circular line represents the boundary of NW1. From Figure 12D it can be observed a high E_x field intensity concentration inside the NW1. Furthermore, we can also observe two side lobes of higher \mathbf{E} field intensity contributing to the absorption improvement of

the design. A considerable amount of E_x field just outside the NW1 is also visible. Figure 12E shows the E_x field intensity along the x - y plane at $z = -404$ nm (inside the substrate, just below NW1) when the operating wavelength is $\lambda = 497$ nm for 3NWs ARC design. The dashed white circular line represents the boundary of NW1. From Figure 12E it can be observed a higher E_x field intensity concentration at the center of the field plot, compared with what was Figure 12B–D, indicating absorption of a larger portion of light. Further to this, we can also observe that two side lobes of lower E_x field intensity than the intensity at the center but also contributing to the absorption improvement of the design.

These figures (i.e., Figures 10–12) suggest that the improvement in the optical performance for a wide range of wavelengths in the case of the two- and three-layered NW ARC designs come from the contribution of the absorption at each of the NWs to the total absorption. It should be noted, all these field plots (i.e., Figures 10–12) are shown at a specific wavelength of 497 nm. Field profiles for resonating mode at different wavelengths are different. Besides that, we have only shown H_y and E_x field profiles and only along some limited number of x - y or x - z planes of a truly 3-dimensional structure.

4 | ELECTRICAL SIMULATIONS SETUP

Although achieving a higher optical absorption may be the initial target, this benefit may not always fully materialize in achieving a similar higher PCE. To calculate

the PCE next, briefly, the total performance of the proposed solar cell is numerically simulated by introducing an electrical model. The basic schematic diagram of the elements used in the computational window for the electrical simulations is shown in Figure 13. The dimensions of the structure are the same as the values used in the optical simulations. Furthermore, the optical generation rate produced in the optical simulation model is imported into the electrical simulation model. The optical generation rate file, which can be generated from the optical simulation file, contains all absorption data as an input for the electrical simulations and it represents the number of photons absorbed by the structure. The generation rate is calculated by multiplying the absorption profile (dependent on wavelength and the spatial x , y , and z coordinates) by the AM1.5 solar spectrum and thus, it contains all absorption data as an input for the electrical model. In Figure 13A, a 3D schematic diagram illustrates the different doping layers under consideration for the simulation using a simple axial pn junction: n-type (n+), intrinsic (p+), and p-type (p++) doped areas. In Figure 13B, a 2D schematic diagram illustrates the different doping layers under consideration for the simulations using a radial pn junction: n+ top layer, n+ side covering all surroundings of NW, p+ doping layer, and p++ doping layer acting as a Back-Surface Field layer. Additionally, two metallic plates (Ag) are placed above and below the structure to act as electrical contacts for the emitter and the base, respectively. The background medium is considered to be Silica (SiO_2). To obtain results as realistic as possible, surface recombination was taken into consideration. Table 1 presents the electrical properties considered for the electrical simulations.

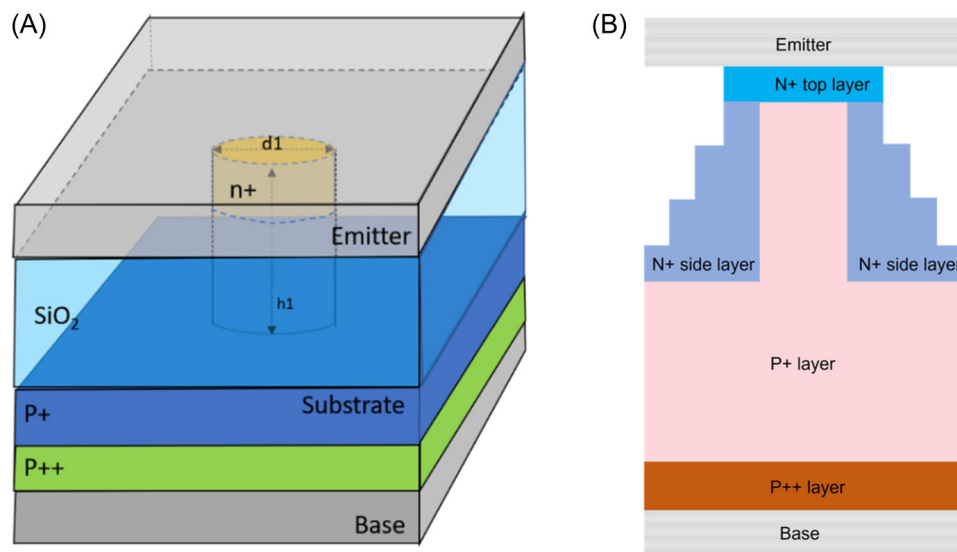


FIGURE 13 Schematic diagram of the setup for the electrical simulation using (A) axial pn junction and (B) radial pn junction.

TABLE 1 Electrical properties considered in the electrical simulations.

Electrical simulation parameters	Values
(μ_p) Hole mobility	$470.5 \text{ cm}^2/\text{Vs}^{52}$
(μ_n) Electron mobility	$1471 \text{ cm}^2/\text{Vs}^{52}$
(N_D) Donor concentration (n+ doping)	$1 \times 10^{+18} \text{ cm}^{-353}$
(N_A) Acceptor concentration (p++ doping)	$1 \times 10^{+19} \text{ cm}^{-354}$
(N_i) Intrinsic (p+ doping)	$1 \times 10^{+15} \text{ cm}^{-354}$
(τ_n) Electron SRH recombination lifetime	$3.3 \mu\text{s}^{55}$
(τ_p) Hole SRH recombination lifetime	$4.0 \mu\text{s}^{55}$
($C_{n \text{ AUGER}}$) Auger recombination of electrons for silicon at 300 K	$2.8 \times 10^{-31} \text{ cm}^6/\text{s}^{56}$
($C_{p \text{ AUGER}}$) Auger recombination of electrons for silicon at 300 K	$9.9 \times 10^{-32} \text{ cm}^6/\text{s}^{56}$
($C_{\text{radiative}}$) Radiative recombination coefficient for silicon at 300 K	$1.6 \times 10^{-14} \text{ cm}^3/\text{s}^{52}$
Surface recombination for electrons and holes at the silver–silicon interface	$1 \times 10^7 \text{ cm/s}^{40}$
Surface recombination for electrons and holes at the silica–silicon interface	100 cm/s^{57}

5 | ELECTRICAL SIMULATION RESULTS AND DISCUSSION

The key electrical parameters, open circuit voltage, open circuit voltage (V_{oc}), and short circuit current, J_{sc} depend on doping and carrier lifetime⁵⁸ and recently we have also discussed their effects for a solar cell using NWs with holes.^{37,38} Variations of the short circuit current density (J_{sc}) with the thickness of the n+ layer for different NW heights are shown in Figure 14A. It can be observed here that all the curves follow a similar trend, the value of J_{sc} is high for thin n+ doping layers but decreases as the n+ layer becomes thicker. For example, in the case of $h_{NW} = 2000 \text{ nm}$, the initial J_{sc} value for a thin n+ layer (25 nm) is 26.7 mA/cm^2 . In any case, it should be highlighted that J_{sc} is higher for taller NWs for the same n+ layer thickness. It can also be noted that for larger NW heights, h_{NW} , the J_{sc} decreases with all the curves experiencing a similar slope as they decrease. For example, for a n+ layer thickness of 200 nm the J_{sc} values for $h_{NW} = 130 \text{ nm}$ is 21.82 mA/cm^2 and for $h_{NW} = 2000 \text{ nm}$ is 25.2 mA/cm^2 . The J_{sc} for two and three layers of NWs mimicking ARC are also shown by orange and brown dashed lines. It can be observed that these J_{sc} values are 6.87% and 13.2% higher than the J_{sc} value for a simple NW of 2000 nm height. It may be possible to increase J_{sc} by using simpler NWs but their heights need to be much higher than 4000 nm.

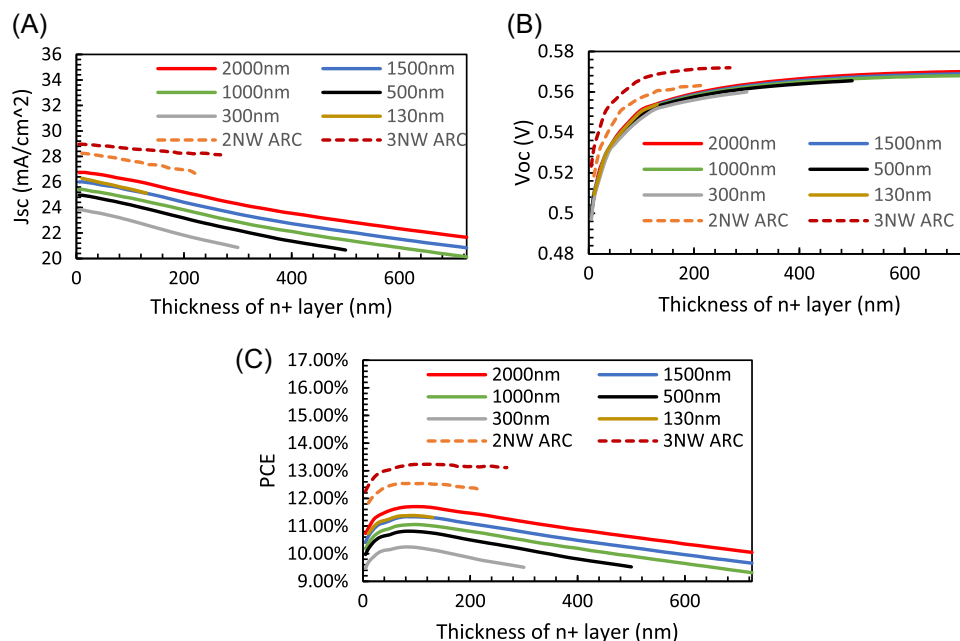


FIGURE 14 (A) Variations of the J_{sc} with the thickness of the n+ layer for different nanowires (NW) heights. (B) Variations of the open circuit voltage (V_{oc}) with the thickness of the n+ layer for different NW heights. (C) Variations of the power conversion efficiency (PCE) with the thickness of the n+ layer for different NW heights.

Similarly, variations of the Voc with the thickness of the n+ layer for different NW heights are shown in Figure 14B. It can be observed that as the n+ layer thickness increases up to 120 nm, there is a rapid increase in the value of Voc (reaching Voc = 0.55 V) in all these cases. It can also be observed that for thicker n+ layers than 120 nm, the increase in the value of Voc is much less pronounced for all the cases. Additionally, in the case of simple NW, all the curves seem to converge to similar Voc values. The Voc values for two and three layers of NWs mimicking ARC are also shown by orange and brown dashed lines. These Voc values are 1.82% and 3.7% higher than in the case of a simple NW of 2000 nm height.

Following the determination of the Jsc and Voc, we calculated the overall performance of the PCE. This parameter can be calculated in terms of Jsc, Voc, FF, P_{OUT}, and P_{IN} where FF is the Fill Factor, P_{OUT} is the output power, and P_{IN} is the input power²⁹:

$$PCE = \frac{P_{OUT}}{P_{IN}} = \frac{J_{SC}V_{OC}FF}{P_{IN}}. \quad (2)$$

Finally, we have shown the PCE_{max} for each of the doping configurations presented here where the P_{OUT} should be equal to the maximum output power (P_{OUTMAX}). Following this condition, the value of FF can be calculated by using the following expression:

$$FF = \frac{P_{OUTMAX}}{J_{SC}V_{OC}}. \quad (3)$$

Variations of the PCE with the thickness of the n+ layer for different NW heights are presented in Figure 14C. It can be observed that the overall performance of the PCE is largely dominated by the performance of the Voc for thin n+ doping layers (until approximately 100 nm thick) since the PCE values rapidly increase. For example, in the case of hNW = 2000 nm, the curve starts at 10.75% for the thin n+ doping layer and rapidly

increases to reach a maximum PCE of 11.7% for a 100-nm-thick n+ doping layer. Then, with further increases in the n+ layer thickness, the PCE values rather start to decrease, and the rate of decrease is very similar in all conventional NW cases. In any case, although the value of PCE decreases for thicker n+ layers, it is possible to achieve a higher PCE value by increasing the hNW while keeping the same n+ thickness. In the cases of two- and three-layer NW ARC, PCE values are shown by orange and brown dashed lines, respectively, and the reduction rate is much slower (especially in the case of three-layer NWs ARC), which may be very useful from the fabrication tolerance point of view. It can also be noted that in the case of two- and two-layer NW, the optimum n+ layer thickness is about 80 nm giving the highest peak PCE values of 12.54% (2NWs) and 13.24% (3NWs). This electrical performance clearly shows that the 2NWs ARC (total height = 220 nm) and 3NWs ARC (total height = 268 nm) offer maximum PCE 7% and 13% higher than that of simple NWs of 2000 nm high. Additionally, it is also important to mention that the similarity in the performance of the simple NWs of hNW = 130 nm and hNW = 1500 nm is shown by dark orange and light blue lines. From the optical simulations shown in Figure 2B, it was found that the performance of a simple NW of hNW = 130 nm would be similar to that of a NW of hNW = 1450 nm.

We have calculated the PCE_{max} for mimicking single-, double-, and triple-layer ARC for both axial and radial dopings and with or without back reflectors. These values are shown in Table 2 along with two representative heights of NWs, 2000 and 4000 nm. It can be noted that in all four cases, PCE_{max} for both two- and three-layer ARC with their total heights of only 220 and 268 nm, respectively, are much higher than what can be achieved with a 4000 nm high NW. It should be noted here that, although a 4000 nm tall NW has a similar TABS value as that of a three-layer ARC with only 268 nm height, its PCE is much lower at 15.64% compared to 17.58% for a three-layer ARC. The resulting

TABLE 2 Power conversion efficiency (PCE) values for various nanowires (NW) designs with axial or radial doping and with or without a back reflector.

NW height (nm)	Total absorption	Axial		Radial	
		No reflector PCE (%)	Reflector PCE (%)	No reflector PCE (%)	Reflector PCE (%)
130	0.718	11.3844	14.2835	12.1527	15.7705
2000	0.842	11.7039	14.1518	12.6450	14.8960
4000	0.871	12.6090	14.6475	13.3288	15.6400
2NWs ARC-220	0.769	12.5436	15.6601	13.4812	16.8260
3NWs ARC-268	0.785	13.2380	16.4338	14.1478	17.5800

PCE reduction in standard taller NWs is due to increased surface recombination loss.^{58–61} Thus, substantial saving of valuable c-Si in fabricating these solar cells is also expected to reduce the cost by adopting the designs presented here mimicking ARC. The benefits of using radial doping and back reflectors have also been shown in Table 2. Further to this, the performance of our designs is also comparable and even superior in some cases, when compared to other texturing patterns when considering a silicon wafer as thin as 4 μm on top of a back reflector. For instance, the random inverted pyramidal presented by considering a back reflector (below a 20- μm -thick silicon substrate), was reported to have a PCE value of 15.5%.¹⁴ The quad-crescent-shaped 2330 nm high silicon NW pattern, is expected to generate a PCE of 16.8% with radial doping and a back reflector.³⁸ A moth eye-inspired texturing pattern yields a PCE value of only 9.76% when considering a 700-nm-thick pattern on top of a 10- μm -thick silicon wafer with a back reflector.⁴⁰ The solar cell with silver nano-cylinder or nano-cube pattern achieved a 6% enhancement in efficiency when considering a 170- μm -thick silicon wafer.⁶² In our design, it is shown that a three-layer NW can achieve 17.58% PCE, one of the highest values so far reported for such a thin solar cell, with a total height of only 268 nm. This trend is a strong validation of our 2NWs and 3NWs ARC designs based on the results obtained from both optical and electrical simulations. The 2NW and 3NW structures can be used to mimic the optical performance of single or multiple ARC layers, which then reflects in strong overall PCE performance.

6 | CONCLUSIONS

Here, to establish our concept of mimicking multiple ARC layers, we have shown our present work for both axial and radial p-n junctions. We have comprehensively analyzed the absorption performance of Si NW solar cells of different shapes. We have shown that the performance of the NW is mostly independent of its shape. We have further explored the performance of short-height NWs (considering the conventional circular shape) and demonstrated excellent performance in this range of heights. Then, we have found evidence of a relationship between this performance and that of the ARC layers. Subsequently, we have used that relationship to mimic an ARC of ideal refractive indices by placing one NW or more than one NW on top of each other. By doing this, we have been able to predict that the higher TABS value of a single NW of height 3450 nm can be achieved by a design of two NWs of diameters $d_1 = 254$ nm and $d_2 = 150$ nm on top of each other with a total height of *only* 220 nm (considering $h_1 = 130$ nm and

$h_2 = 90$ nm). Similarly, the TABS value of a single NW of height 4270 nm can be achieved by using three NWs of diameters $d_1 = 272$ nm, $d_2 = 203$ nm, and $d_3 = 116$ nm on top of each other with a total height of *only* 268 nm (considering $h_1 = 91$ nm, $h_2 = 88$ nm, and $h_3 = 89$ nm). Furthermore, this strong optical performance has been validated by excellent performance from the electrical simulations. Although optical simulations of a two-layer ARC design reported here can give a similar TABS value as that of standard NWs of 3450 nm high, additional electrical simulations show that this design even outperforms Si solar cells using NWs of 4000 nm high, as shown in Table 2. The reduced electrical performance of a taller NW can be attributed to increased surface recombination loss.⁶⁰ This clearly shows that our design with a total height of only 268 nm yields higher PCE values and significantly outperforms even a very tall 4000 nm high NW, with greater than one order of magnitude thickness reduction. This is a large improvement in terms of optical absorption that can benefit from an electrical performance with low surface recombination due to the low surface-to-volume ratio of the design. Therefore, our proposed designs of using two and three layers of NWs can be used to mimic the performance of an ARC of ideal refractive index value without the need to have a material with a matching refractive index value over the whole wavelength range of the solar spectrum. The fabrication process required for these dispersion-independent designs has been reported,^{31,51} which will consume less material, less waste of valuable Si, and ultimately lower costs as etching less than 300 nm can be carried out faster than compared to a 4000 nm high NW, more than one order of further height reduction. Also, bear in mind that in the case of taller NWs, it may be difficult to have an exactly vertical or uniform cross-section, which may deteriorate the actual PCE compared to its expected PCE. The fabrication process needed here has been reported for both Silicon³¹ and Ge⁵¹ solar cells and we expect that this concept can be used in PVSC using other semiconductor materials for multi-junctions, such as Si with GaAs or perovskite tandem solar cells. Similarly, this concept can be applied to other innovative approaches, such as using a thin graphene layer to increase absorption further⁶³ or energy downshifting to absorb more solar energy from a wider solar spectrum.⁶⁴ We believe that the performance of these designs can be further enhanced by using even a much thinner layer by adopting the concept of mimicking multiple ARC layers presented here by using NWs of different diameters while reducing material waste and costs.

ACKNOWLEDGMENTS

Project funded by the MSCA Horizon 2020 program. Project acronym: SolArray. Grant No: 101032153.

DATA AVAILABILITY STATEMENT

The data that support the findings of this study are available on request from the corresponding author. The data are not publicly available due to privacy or ethical restrictions.

ORCID

Francisco J. Cabrera-España  <http://orcid.org/0000-0001-7915-0711>

B. M. Azizur Rahman  <https://orcid.org/0000-0001-6384-0961>

REFERENCES

1. The White House: Office of the Press Secretary. *FACT SHEET: Renewed U.S. Leadership in Glasgow Raises Ambition to Tackle Climate Crisis*. <https://www.whitehouse.gov/briefing-room/statements-releases/2021/11/13/fact-sheet-renewed-u-s-leadership-in-glasgow-raises-ambition-to-tackle-climate-crisis/>
2. United Nations: Framework Convention on Climate Change. *Report of the Conference of the Parties on its Twenty-Sixth Session, Held in Glasgow from 31 October to 13 November 2021*. https://unfccc.int/sites/default/files/resource/cp2021_12_adv.pdf
3. European Commission. *The European Green Deal*. https://ec.europa.eu/commission/presscorner/detail/en/fs_21_3688
4. Hunt G, Macfarlane I. *Certainty and Growth for Renewable Energy*. <http://www.environment.gov.au/minister/hunt/2015/mr20150623.html>
5. Solangi KH, Islam MR, Saidur R, Rahim NA, Fayaz H. A review on global solar energy policy. *Renew Sustain Energy Rev*. 2011;15(4):2149-2163.
6. Khattak CP, Ravi KV. *Silicon Processing for Photovoltaics*. North-Holland Physics Publishing; 1985.
7. Krebs FC. *Polymer Photovoltaics: A Practical Approach*. SPIE Press; 2008.
8. European Commission. *COMMISSION STAFF WORKING DOCUMENT Annual Single Market Report 2021*. <https://eur-lex.europa.eu/legal-content/en/TXT/?uri=CELEX%3A52021SC0351>
9. Archer MD, Green MA. *Clean Electricity from Photovoltaics*. Imperial College Press; 2015.
10. Green MA, Dunlop ED, Siefer G, et al. Solar cell efficiency tables (Version 61). *Prog Photovoltaics Res Appl*. 2023;31(1):3-16. doi:10.1002/pip.3646
11. Powell DM, Winkler MT, Goodrich A, Buonassisi T. Modeling the cost and minimum sustainable price of crystalline silicon photovoltaic manufacturing in the United States. *IEEE J Photovolt*. 2013;3:662-668. <https://ieeexplore.ieee.org/document/6407638>
12. Zhu L, Zou S, Ni M, et al. Ultrafast random-pyramid texturing for efficient monocrystalline silicon solar cells. *Solar RRL*. 2022;6:2200204. doi:10.1002/solr.202200204
13. Manzoor S, Filipič M, Onno A, Topič M, Holman ZC. Visualizing light trapping within textured silicon solar cells. *J Appl Phys*. 2020;127:063104.
14. Hwang I, Jeong Y, Shiratori Y, et al. Effective photon management of non-surface-textured flexible thin crystalline silicon solar cells. *Cell Rep Phys Sci*. 2020;1:100242.
15. Dalmau Mallorquí A, Epple FM, Fan D, Demichel O, Fontcuberta i Morral A. Effect of the pn junction engineering on Si microwire-array solar cells. *Phys Status Solidi A*. 2012;209(3):1588-1591. doi:10.1002/pssa.201228165
16. Singh VK, Nagaraju J, Avasthi S. Radial junction silicon solar cells with micro-pillar array and planar electrode interface for improved photon management and carrier extraction. *Curr Appl Phys*. 2019;19(3):341-346. doi:10.1016/j.cap.2018.12.016
17. Garnett E, Yang P. Light trapping in silicon nanowire solar cells. *Nano Lett*. 2010;10:1082-1087. doi:10.1021/nl100161z
18. Kordrostami Z, Shekholeslami H. Optimization of light trapping in square and hexagonal grid inclined silicon nanowire solar cells. *Opt Commun*. 2020;459:124980. doi:10.1016/j.optcom.2019.124980
19. Saive R. Light trapping in thin silicon solar cells: a review on fundamentals and technologies. *Prog Photovoltaics Res Appl*. 2021;29(10):1125-1137. doi:10.1002/pip.3440
20. Gao Y, Cansizoglu H, Polat KG, et al. Photon-trapping microstructures enable high-speed high-efficiency silicon photodiodes. *Nat Photonics*. 2017;11:301-308. doi:10.1038/nphoton.2017.37
21. Lee HS, Choi JM, Jung B, et al. Random nanohole arrays and its application to crystalline Si thin foils produced by proton induced exfoliation for solar cells. *Sci Rep*. 2019;9:19736. doi:10.1038/s41598-019-56210-7
22. Raad SH, Atlasbaf Z. Solar cell design using graphene-based hollow nano-pillars. *Sci Rep*. 2021;11:16169. doi:10.1038/s41598-021-95684-2
23. Atwater HA, Polman A. Plasmonics for improved photovoltaic devices. *Nat Mater*. 2010;9:205-213. doi:10.1038/nmat2629
24. Ai B, Fan Z, Wong ZJ. Plasmonic-perovskite solar cells, light emitters, and sensors. *Microsyst Nanoeng*. 2022;8(5):5. doi:10.1038/s41378-021-00334-2
25. Park KT, Guo Z, Um H-D, et al. Optical properties of Si microwires combined with nanoneedles for flexible thin film photovoltaics. *Opt Express*. 2011;19(101):A41. doi:10.1364/OE.19.000A41
26. Yablonovitch E, Cody GD. Intensity enhancement in textured optical sheets for solar cells. *IEEE Trans Electron Devices*. 1982;29:300-305.
27. Lee K, Hwang I, Kim N, et al. 17.6% efficient radial junction solar cells using silicon nano/micro hybrid structures. *Nanoscale*. 2016;8:14473-14479. doi:10.1039/C6NR04611H
28. Choi D, Hwang I, Lee Y, Lee M, Um HD, Seo K. Wafer-scale radial junction solar cells with 21.1% efficiency using c-Si microwires. *Adv Funct Mater*. 2022;32:2208377. doi:10.1002/adfm.202208377
29. Cabrera España FJ. *Analysis of the optical properties of texturing patterns for design of Si solar cells*. PhD thesis City, University of London, London; 2017.
30. Wang J, Li Z, Singh N, Lee S. Highly-ordered vertical i nanowire/nanowall decorated solar cells. *Opt Express*. 2011;19(23):23078. doi:10.1364/OE.19.023078
31. Wendisch FJ, Abazari M, Mahdavi H, et al. Morphology-graded silicon nanowire arrays via chemical etching: engineering optical properties at the nanoscale and macroscale. *ACS Appl Mater Interfaces*. 2020;12(11):13140-13147. doi:10.1021/acsami.9b21466

32. Lu Y, Lal A. High-efficiency ordered silicon nano-conical-frustum array solar cells by self-powered parallel electron lithography. *Nano Lett.* 2010;10(11):4651-4656. doi:10.1021/nl102867a
33. Yu S-Q, Kupec J, Witzigmann B. Electro-optical modeling of InP nanowire solar cells: Core-shell vs. axial structure. In Proceedings of the 10th International Conference on Numerical Simulation of Optoelectronic Devices (NUSOD) 2010, 57-58. doi:10.1109/NUSOD.2010.5595667
34. Li Z, Tan HH, Jagadish C, Fu L. III-V semiconductor single nanowire solar cells: a review. *Adv Mater Technol.* 2018;3:1800005. doi:10.1002/admt.201800005
35. Kayes BM, Atwater HA, Lewis NS. Comparison of the device physics principles of planar and radial p-n junction nanorod solar cells. *J Appl Phys.* 2005;97:114302.
36. Raj V, Tan HH, Jagadish C. Axial vs radial junction nanowire solar cell. *Asian J. Phys.* 2021;28(7-9):719-746.
37. Lundgren C, Lopez R, Redwing J, Melde K. FDTD modeling of solar energy absorption in silicon branched nanowires. *Opt Express.* 2013;21:A392-A400. doi:10.1364/OE.21.00A392
38. El-Bashar R, Hussein M, Hegazy SF, et al. Electrical performance of efficient quad-crescent-shaped Si nanowire solar cell. *Sci Rep.* 2022;12(48):48. doi:10.1038/s41598-021-03597-x
39. Mahmoud AHK, Hameed MFO, Hussein M, Obayya SSA. Optical and electrical characteristics of highly efficient flower-shaped silicon nanowires solar cell. *Opt Quantum Electron.* 2023;55:341. doi:10.1007/s11082-022-04481-2
40. Gao Z, Lin G, Chen Y, et al. Moth-eye nanostructure PDMS films for reducing reflection and retaining flexibility in ultrathin c-Si solar cells. *Sol Energy.* 2020;205:275-281.
41. Taflove A. *Advances in FDTD Computational Electrodynamics: Photonics and Nanotechnology.* Artech House; 2013.
42. Lumerical Solutions, Inc., Ansys Canada Ltd; 2023. <http://www.lumerical.com>
43. Rahman BMA, Agrawal A. *Finite Element Modeling Methods for Photonics.* Artech House; 2013.
44. Palik ED. *Handbook of Optical Constants of Solids.* Academic Press; 1985.
45. Halir R, Bock PJ, Cheben P, et al. Waveguide sub-wavelength structures: a review of principles and applications. *Laser Photon Rev.* 2014;9(1):25-49. doi:10.1002/lpor.201400083
46. Phillips BM, Jiang P. *Biomimetic Antireflection Surfaces.* Elsevier; 2013.
47. Priyadarshini BG, Sharma AK. Design of multi-layer anti-reflection coating for terrestrial solar panel glass. *Bull Mater Sci.* 2016;39(3):683-689. doi:10.1007/s12034-016-1195-x
48. Hu Y, Li M, He J-J, LaPierre RR. Current matching and efficiency optimization in a two-junction nanowire-on-silicon solar cell. *Nanotechnology.* 2013;24(6):065402. doi:10.1088/0957-4484/24/6/065402
49. Kupec J, Stoop RL, Witzigmann B. Light absorption and emission in nanowire array solar cells. *Opt Express.* 2010; 18(26):27589-27605.
50. Yan X, Gong L, Ai L, Wei W, Zhang X, Ren X. Enhanced photovoltaic performance of nanowire array solar cells with multiple diameters. *Opt Express.* 2018;26:A974-A983.
51. Fan Z, Kapadia R, Leu PW, et al. Ordered arrays of dual-diameter nanopillars for maximized optical absorption. *Nano Lett.* 2010;10(10):3823-3827. doi:10.1021/nl1010788
52. Lin C. *Analysis and Simulation of Semiconductor Devices.* Springer; 2012.
53. Li Z, Wenas YC, Fu L, Mokkaapati S, Tan HH, Jagadish C. Influence of electrical design on core-shell GaAs nanowire array solar cells. *IEEE J Photovolt.* 2015;5(3):854-864.
54. Fossum JG. Physical operation of back-surface-field silicon solar cells. *IEEE Trans Electron Dev.* 1977;24(4):322-325.
55. Varker CJ, Whitfield JD, Fejes PL. *Silicon Processing.* ASTM International; 1983.
56. Lutz J, Schlangenotto H, Scheuermann U, De Doncker R. *Semiconductor Power Devices Physics, Characteristics, Reliability.* Springer; 2011.
57. Deinega A, Eyderman S, John S. Coupled optical and electrical modeling of solar cell based on conical pore silicon photonic crystals. *J Appl Phys.* 2013;113:224501.
58. Branham MS, Hsu WC, Yerci S, et al. 15.7% efficient 10- μ m-thick crystalline silicon solar cells using periodic nanostructures. *Adv Mater.* 2015;27:2182-2188. doi:10.1002/adma.201405511
59. Thiyagu S, Fukata N. *Silicon Nanowire-Based Solar Cells. I Nanomaterials for Solar Cell Applications.* Elsevier; 2019: 325-348.
60. Da Y, Xuan Y. Role of surface recombination in affecting the efficiency of nanostructured thin-film solar cells. *Opt Express.* 2013;21:A1065-A1077. doi:10.1364/OE.21.0A1065
61. Kang SB, Park WJ, Jeong MH, Kang S-H, Yang C, Choi KJ. Ambipolar passivated back surface field layer for silicon photovoltaics. *Adv Funct Mater.* 2020;30:2004943. doi:10.1002/adfm.202004943
62. Birant G, Ozturk IM, Doganay D, Unalan HE, Bek A. Plasmonic light-management interfaces by polyol-synthesized silver nanoparticles for industrial scale silicon solar cells. *ACS Appl Nano Mater.* 2020;3(12):12231-12239. doi:10.1021/acsnm.0c02694
63. El-Rashidi A. Light harvesting in silicon nanowires solar cells by using graphene layer and plasmonic nanoparticles. *Appl Sci.* 2022;12(5):2519. doi:10.3390/app12052519
64. Kim HT, Lee K, Jin W, et al. Phosphorescent energy downshifting for diminishing surface recombination in silicon nanowire solar cells. *Sci Rep.* 2018;8:16974. doi:10.1038/s41598-018-35356-w

How to cite this article: Cabrera-España FJ, Kamuka A, Khaled A, Hameed MFO, Obayya SSA, Rahman BMA. Optical and electrical characterization of solar cell with nanowires mimicking antireflection coating layers considering axial and radial PN junctions. *Energy Sci Eng.* 2024;1-17. doi:10.1002/ese3.1722